Transport of nanoparticulate TiO2 UV-filters through a saturated sandcolumn at environmentally relevant concentrations

Sylvie Motellier, Amandine Arnould, Dominique Locatelli, Jérôme Labille

Transport of nanoparticulate TiO_2 UV-filters through a saturated sand column at environmentally relevant concentrations

Sylvie Motellier[1]*, Amandine Arnould[1], Dominique Locatelli[1], and Jérôme Labille[2]

[1] Univ. Grenoble Alpes, CEA, LITEN, DTNM, STDC, Laboratory of Measure, Safety, and Environment, 38000 Grenoble, France

[2] Aix Marseille Univ, CNRS, IRD, INRAE, Coll France, CEREGE, Aix-en-Provence, France

Keywords : Titanium dioxide, nanoparticle, sunscreen, UV filter, transport, porous medium

Abstract

The fate of sunscreen residues released during bathing activities around recreational areas is an emerging concern regarding the potential ecotoxicity of some of their ingredients, including nanoparticulate TiO_2 UV-filters. To assess the extent of contamination in the natural medium, sand-packed column experiments were carried out with bare TiO_2 engineered nanoparticles (ENPs) and two commercial nano-TiO_2 UV-filters coated with either SiO_2 (hydrophilic) or a combination of Al_2O_3 and simethicone (amphiphilic). The high sensitivity of (single particle)ICPMS online monitoring of the breakthrough curves made it possible to inject the ENPs at trace levels (2 - 100 µg L^{-1}) in eluents composed of 10^{-3} and 10^{-2} M NaCl and pHs of 5.7 and 7.8. The deposition of all ENPs in the sand increased with the ionic strength and decreased with the pH of the carrier. Both bare and SiO_2-coated ENPs showed a clear control by the electrostatic interactions between the particles and the quartz grains surfaces, in partial agreement with classical DLVO theory. Unexpectedly high rates of transfer were observed with the amphiphilic UV-filter, which could be explained by the addition of a contribution to the DLVO model to account for the steric repulsion between the sand collector and the

polysiloxane surface layer of this ENP. These results demonstrate the major role played by the coating of UV-filters regarding their fate in porous media like soils, sediments and aquifers.

1. Introduction

Due to the skin damages induced by sunbathing, extensive topical application of suncare products in recreational areas is prevalent nowadays. A recent survey among beachgoers in southern France revealed that almost 70% of them use sunscreens and more than 75% have a bath when they go to the beach (Labille, Slomberg*, et al.*, 2020). Depending on the category, from waterproof to no claim labelling, 10 to 90% of suncare products applied on the skin are expected to be washed off into the bathing water (Stokes & Diffey, 1999). Based on consumer use, sunscreen production, and a mean release of 25% in seawater, Danovaro et al. estimated that 4,000 to 6,000 t/y of sunscreens could be discharged worldwide in reef areas (Danovaro *et al.*, 2008). Beside direct release, sunscreen residues may also be washed off the body after washing and end up in the sewage system (Johnson *et al.*, 2011). This extensive usage of suncare products has raised an environmental concern with regard to the occurrence of sunscreen ingredients having possible adverse effects on aquatic ecosystems (sea-, river-, and lakeshores) (Labille, Catalano*, et al.*, 2020).

Titanium dioxide (TiO_2) and zinc oxide (ZnO) engineered nanoparticles (ENPs) are commonly used as mineral UV-filters because of their ability to scatter and absorb UVA and UVB radiations (Osterwalder *et al.*, 2014). However, they belong to the disputed ingredients with suspected deleterious effects on benthic organisms (Li *et al.*, 2014), plankton, algae, etc. (Sendra *et al.*, 2017, Sánchez-Quiles & Tovar-Sánchez, 2014, Tovar-Sánchez *et al.*, 2013). A predicted no effect concentration (PNEC) value of 1 µg L^{-1} of TiO_2 on aquatic organisms was proposed by Mueller and Nowack (Mueller & Nowack, 2008). In river and lake waters, the colloidal TiO_2 concentration range was found to be 0.1 – 30 µg L^{-1} (Johnson *et al.*, 2011, Gondikas *et al.*, 2014, Venkatesan *et al.*, 2018, Gottschalk *et al.*, 2013), exceeding the proposed PNEC, and Ti-containing particle concentrations were always correlated to the bathing

activities in the investigated recreational areas, with up to an 80% increase of suspended particles (aggregates 100-500 nm in size) during peak activity compared to the background level (Gondikas *et al.*, 2014, Venkatesan *et al.*, 2018). In a one-year survey of an Austrian recreational lake, Gondikas et al. measured an overall 40% increase in the number of suspended particles containing Ti during the summer season (Gondikas *et al.*, 2018). Notably, extra Ti-containing particles (compared to the background level measured off-season) persisted in the water for a few weeks after the bathing season, in coherence with submicron TiO_2 colloids stability observed after in-laboratory exposure of water-dispersed sunscreens to light (Labille *et al.*, 2010, Botta *et al.*, 2011). The sediment top layer was enriched in TiO_2 particles of anthropogenic origin at different locations of the lake away from the bathing areas. Despite the low circulation of this type of fresh water, these observations support the occurrence of a dispersion process of the ENPs before their settlement onto the bottom of the lake. Bioturbation of the sediment and its re-suspension by bathers may also contribute to the migration of Ti-containing particles to remote places, as hypothesized by Reed et al. to explain the observed increase in Ti concentration in the water downstream a natural waterway recreational site in Colorado during the peak activity (Reed *et al.*, 2017). A decrease of the Ti-bearing particle concentration with depth in the water column concurrently with transient adhesion of the TiO_2 NPs to the air-water interface was also revealed by Gondikas et al. (Gondikas *et al.*, 2018), and similar concentration profiles of TiO_2 with depth were reported by Labille et al. in marine waters close to a beach in Southern France, with 100–900 µg L^{-1} TiO_2 at the water surface and 20–50 µg L^{-1} in the water column underneath (Labille, Slomberg, *et al.*, 2020). Lake waters with poor natural organic matter favor TiO_2 ENP suspension in the water column for longer times than highly saline waters (brines and sea waters) where rapid sedimentation of TiO_2 ENPs is promoted (Botta *et al.*, 2011, Li *et al.*, 2016).

Whether they are deposited onto the bottom of the lake/river/sea or remain in suspension, nanoparticulate TiO_2 will eventually experience filtration through the porous medium they encounter. In a life cycle release study, Keller et al. estimated that 33 to 44 % of the emission of engineered nanomaterials from cosmetic applications would end up in soils after initial release to water (Keller *et*

al., 2013). The transport and deposition processes of TiO_2 ENPs through different soils are commonly addressed via labscale experiments involving columns packed with granular (mainly sandy) stationary beds. Studies on that topic describe the role of the porous collector (grain size and heterogeneity (Lv *et al.*, 2016), soil nature and integrity (Fang *et al.*, 2009, Ollivier *et al.*, 2018, Cary *et al.*, 2015)) and the eluent characteristics (chemistry (Petosa *et al.*, 2012, Chen *et al.*, 2011, 2012, Cai *et al.*, 2014), ionic strength (Chowdhury *et al.*, 2011, Chen *et al.*, 2011, 2012, Petosa *et al.*, 2012), and velocity (Chowdhury *et al.*, 2011, Ollivier *et al.*, 2018)) on the fate of TiO_2 NPs. They show that deposition of the particles in the porous medium is essentially governed by competitive particle-particle or particle-collector surface interactions. Most studies deal with the transport behavior of bare TiO_2 ENPs and only few of them point out the role of particle coating, although it is one of the primary features that govern the particle surface properties and, consequently, the colloidal stability and interactions with the collector. This point was demonstrated by Petosa et al. who compared the transfer of bare and polyacrylic acid-functionalized TiO_2 ENPs in a sand-packed column (Petosa *et al.*, 2012). The authors found that the surface-modified NPs were significantly more stable in suspension and more mobile in the porous medium than their bare counterparts, even at high ionic strength (10^{-1} M). They attributed this difference in behavior to the increase in the negative surface charge induced by the polymer coating, thereby promoting both inter-particle and particle-sand repulsions at the pH of the experiments. Enhanced mobility was also reported with carboxymethylcellulose-encapped TiO_2 nanoparticles (Joo *et al.*, 2009).

Nanoparticulate TiO_2 UV-filters contained in sunscreens are in the least photocatalytic rutile crystalline form (Lewicka *et al.*, 2011) and their surface is always modified to i) mitigate their remaining photoactivity and prevent skin damage mediated by oxidative stress and ii) favor their dispersion in the formulation which, in turn, increases their performance as UV-filter (Faure *et al.*, 2013, Catalano *et al.*, 2021). Alumina (Al_2O_3), silica (SiO_2), and a combination of these minerals with polymers are common coating layers because they are inert and biocompatible, they efficiently photopassivate the

100 TiO_2 ENPs (Johnston *et al.*, 2009), and they can tune the surface characteristics of the particles (charge,
101 hydrophobicity) to promote better compatibility with the cream/lotion matrix (Catalano *et al.*, 2020).

102 In order to clarify the influence of particle coating on the transfer of nanoparticulate TiO_2 UV-filters
103 through the soil compartment, flow-through experiments were carried out with two TiO_2-coated ENPs
104 commonly used in sunscreen formulations. Their coating was either hydrophilic for enhanced
105 dispersion in the water phase of the sunscreen emulsion or amphiphilic for dispersion enabled in both
106 the water and the oil phases. A moderately hydrophilic bare TiO_2 ENP was used as reference material.
107 The suspensions were injected in a saturated sand column and the breakthrough curves (BTCs) of Ti
108 were monitored using online inductively coupled plasma-mass spectrometry (ICPMS) operated either
109 in standard or in single particle (sp) mode, the latter being successfully applied to the detection and
110 characterization of Ti-containing particles in recreational waters (Venkatesan *et al.*, 2018). Continuous
111 online detection with these highly sensitive techniques allowed the injection of ENPs at concentrations
112 in the µg L^{-1} level (Motellier *et al.*, 2019), thereby limiting the risk of unrealistic retention processes
113 (like blocking) when higher concentration step inputs are performed (Peijnenburg *et al.*, 2016). The
114 carrier pH and ionic strength were varied to observe the distinct behavior of the UV-filters in
115 environmentally-relevant conditions. The two chosen pHs, 5.7 and 7.8, refer to slightly acidic soft
116 surface- or groundwaters and to slightly alkaline fresh and marine waters (Nikanorov & Brazhnikova,
117 2009). Sodium chloride (NaCl) at the concentration of 10^{-3} and 10^{-2} M was used as simple 1:1 carrier
118 electrolyte intended to approach the composition of marine and estuarine waters, or surface waters
119 containing high total dissolved solids for which aggregation and sedimentation rates are substantial
120 (Keller *et al.*, 2010). The experimental results were clarified by considering the colloid filtration and
121 Derjaguin-Landau-Verwey-Overbeek (DLVO) theories, including steric interactions generated by
122 compressible particle coating when relevant.

123

2. Materials and methods

2.1. TiO_2 suspension, carrier, and sand preparation

Three TiO_2 ENPs were selected in this study. A TiO_2 ENP in the powder form (Aldrich) was used as reference (rutile, primary size < 100 nm). It will be referred to as T_{rutile}. The two other ENPs were commercial nanoparticulate TiO_2 UV-filters commonly found in sunscreens. The first one was composed of a TiO_2 core coated with amorphous silica (Eusolex® T-AVO powder from Merck, rutile (79.6%)/SiO_2); it was selected for its enhanced hydrophilicity compared to bare TiO_2 and will be referred to as T_{hydro}. The second UV-filter consisted in a TiO_2 core coated with an inner shell of alumina and a second outer layer of simethicone, which is a combination of polydimethylsiloxane (PDMS) and ca. 5% silica (Eusolex® T-2000 powder from Merck, rutile (80.3%)/Al_20_3/simethicone); it was selected for the amphiphilic nature of its surface and will be referred to as T_{amphi}. The samples were prepared in polypropylene tubes by dilution of the daily-made stock suspension (1 g L^{-1} in ultrapure water (UP)) in the eluent immediately prior to each injection to avoid adsorption onto the vessel wall. Sodium bromide (NaBr, Sigma-Aldrich) was added to the injected samples to monitor the conservative tracer Br^- simultaneously. All suspensions were sonicated during 5 min for homogenization in an US cleaner (Branson) prior to injection. The injected samples were composed of the TiO_2 ENPs at a concentration of 100 µg L^{-1} and NaBr at a concentration of 700 µg L^{-1} (Br^- concentration of 550 µg L^{-1}) in the eluent when the BTCs were monitored by ICPMS. NaBr was omitted and the concentration of the ENPs was decreased to 2 µg L^{-1} when the BTCs were monitored using spICPMS. The eluent was composed of NaCl (Sigma-Aldrich) in UP water at two different concentrations (10^{-3} M and 10^{-2} M). It was filtered at 0.4 µm and was either used without further treatment (pH = 5.7 ± 0.2) or buffered at pH 7.8 ± 0.2 by addition of 4-(2-hydroxyethyl)-1-piperazineethanesulfonic acid (HEPES, 2 10^{-4} M in 10^{-3} M NaCl and 2 10^{-3} M in 10^{-2} M NaCl) and pH adjustment with 0.1 M NaOH (Merck).

The Hostun sand (HN34, composed of quartz (> 98%), metal oxides, and kaolin) was purchased from Sika. It was sieved between 200 and 400 µm (median grain size $d_{50,collector}$ = 235 µm) and cleaned to

149 remove its impurities by successive rinsing in 1 M HCl and 1 M NaOH. The pore size distribution (10 to
150 200 µm) was centered at 65 µm; the BET surface area was 0.53 $m^2 g^{-1}$ (Vitorge, 2010) according to the
151 process described in SI. Additional information on the characteristics of the sand is provided in Table
152 S1 (SI).

153

154 ## 2.2. Column experiments

155 The setup was composed of an inert IC pump (Dionex), an inert 6-way valve injector (Hamilton) with a
156 4.25 mL PTFE injection loop (~ 9 pore volumes), a glass column (0.66 cm internal diameter and
157 adjustable bed length, Omnifit, Sigma-Aldrich), and an inductively coupled plasma-mass spectrometer
158 (ICPMS 7900, Agilent Technologies). The column was filled with 1.5 g of dry sand (~3 cm in length) that
159 was renewed before each experiment and equilibrated with the eluent for at least 40 pore volumes.
160 The gravimetrically determined porosity was 44 ± 2%. The eluent flow rate was set at 0.5 mL min^{-1},
161 generating a Darcy velocity of 0.026 cm s^{-1} and a pore velocity of 0.06 cm s^{-1}. The BTCs were monitored
162 online by direct coupling of the column outlet to the ICPMS sample introduction system using either
163 the standard time-resolved analysis (TRA) mode or the sp mode of the ICPMS. The experimental
164 conditions for these two modes are listed in Table S2. In the standard TRA mode, ^{47}Ti, ^{27}Al, ^{29}Si (ENP
165 constituents), ^{79}Br (conservative tracer), and ^{37}Cl (eluent) were monitored simultaneously. In sp mode,
166 only ^{47}Ti was recorded with a dwell time of 3 ms during 1 min runs. All BTCs are presented as corrected
167 signals expressed from Eq. S1 in SI.

168 Each attachment experiment was a two-stage process. First, the sample was injected into the setup
169 where the column was replaced by a zero-volume junction. Then, it was injected again in the setup
170 with the packed column. The fraction of particles retained on the sand was calculated by the ratio of
171 the ICPMS signals on the plateau of the BTCs with and without the column in the system. For ease of
172 comparison, the signals were normalized according to the calculation described in SI. All experiments
173 were performed in triplicate.

2.3. Characterization techniques

Dynamic light scattering (DLS, ZetaSizer Nano ZSP, Malvern Instruments) was used for the measurement of the hydrodynamic diameter (D_h, number mean) and the zeta potential (ZP) of the ENPs. ZP of the sand was determined using the streaming potential method (Surpass, Anton Paar). Transmission electron microscopy (TEM, Tecnai Osiris, FEI) and scanning electron microscopy (SEM, S5500, Hitachi), both equipped with an energy dispersive X-ray spectroscopy (EDS) detector, were used to image the pristine ENPs and their attachment to the sand, respectively. SEM observations of the ENP attachment to the sand were performed in 10^{-2} M NaCl at pH 5.7 with specific batch experiments involving a higher ENP concentration (5 mg L^{-1}) compared to the concentration used for the attachment tests to detect a significant number of particles on the sand. The experimental procedures related to these characterization techniques are described in SI.

2.4. Attachment Efficiency and interaction energy profiles

Particle deposition in a porous medium can be quantified by calculation of the particle/collector attachment efficiency α from the filtration theory (Tufenkji & Elimelech, 2004). This parameter accounts for the fraction of collisions between particles and sand grains which result in particle deposition. It is defined as:

$$\alpha = \frac{\eta}{\eta_0} = -\frac{2d_c}{3(1-f)L\eta_0}\ln(\frac{C}{C_0}) \qquad \text{(Eq. 1)}$$

Where η is the single-collector removal efficiency, η_0 is the single-collector contact efficiency (expression in SI), d_c is the collector diameter, f is the medium porosity, and L is the column length. C/C_0 is the ratio between the corrected signals on the plateau of the BTCs from the experiment performed with the sand-packed column and that without column.

The maximum distance L_{max} of ENP transport in the porous medium can be derived from Eq. 1 by considering that L_{max} is reached when 99.9% of the colloids are retained in the medium (i.e. for C/C_0 = 0.001) (Fang *et al.*, 2009, Godinez & Darnault, 2011).

198 The ENP-sand grain interaction energy profile was calculated from the DLVO theory as the sum of the
199 electrostatic interaction energy (E_{El}), which can be either attractive or repulsive depending on the
200 potentials of the approaching surfaces, the van der Waals attractive energy (E_{VdW}), and the short-range
201 Born repulsion reflecting the overlap of electron orbitals (E_{Born}).

202 $$E_s = E_{El} + E_{VdW} + E_{Born} \quad \text{(Eq. 2)}$$

203 The steric interaction generated by the occurrence of the simethicone coating in the case of T_{amphi} was
204 depicted by an additional contribution (E_{steric}) in the total interaction energy (Byrd & Walz, 2005,
205 Bradford *et al.*, 2021):

206 $$E_{s\,(Tamphi)} = E_{El} + E_{VdW} + E_{Born} + E_{steric} \quad \text{(Eq. 3)}$$

207 Considering that PDMS is a viscoelastic material composed of a flexible siloxane backbone with side
208 methyl groups (de Buyl, 2001), the calculation of E_{steric} was approximated by modeling the grafted
209 simethicone external layer of T_{amphi} as a polymer brush surface.

210 The mathematical expressions of the interaction energies are detailed in SI along with the Hamaker
211 constants and surface potentials taken from the literature (Tables S3 and S4).

212

213 # 3. Results and discussion

214 ## 3.1. Particle characterization

215 The particles were characterized prior to their injection into the sand column. TEM images of the three
216 ENPs dispersed in UP water (pH ~ 5.7) are provided in Fig. 1 and Fig. S1 (in SI). The ENPs were ca. 60
217 nm in length. T_{rutile} primary particles were elongated spheroids. T_{hydro} formed nanorods and T_{amphi}
218 formed needle-like particles. The three ENPs were agglomerated or aggregated in small clusters, with
219 preferentially aligned particles in the case of the two UV-filters. The estimate of the thickness of the
220 coating layers was assessed by EDS mapping (Fig. S2 and Fig. S3). The thickness of the silica coating of

221 T_{hydro} was ca. 6 nm. The alumina inner layer and the simethicone outer coating of T_{amphi} were estimated
222 to be 3 nm and 7 nm in thickness, respectively, in good agreement with the mass-based composition
223 of the ENPs provided by the supplier and the organic coating mass contribution measured by Catalano
224 et al. (Catalano *et al.*, 2020).

225 DLS measurements confirmed that the primary particles of all three nanocolloids were agglomerated
226 in suspension at the mg L^{-1} concentration level, with hydrodynamic diameters ranging from 90 to 260
227 nm depending on the pH and ionic strength conditions (Fig. S4 and Table 1). Contrary to T_{rutile} and T_{hydro}
228 which agglomeration states were independent of the pH and ionic strength in the investigated ranges,
229 D_h of T_{amphi} was larger in 10^{-2} M NaCl than in 10^{-3} M NaCl at pH 5.7, which could be attributed to a
230 favorable agglomeration process induced by a higher salt concentration in the medium. Labille et al.
231 determined the critical coagulation concentration (ccc) of a UV-filter of composition close to that of
232 T_{amphi} (rutile/Al_2O_3/dimethicone) to be 2 10^{-2} M NaCl at pH 6.3 (Labille *et al.*, 2010). In addition, the ccc
233 of rutile nanorods (40 to 120 nm primary length) was measured at ~ 7 10^{-2} M NaCl at pH 8.0 (Zhou *et*
234 *al.*, 2013), and that of anatase (30 nm primary length) at 2.5 10^{-2} M NaCl at pH 5.0 (Labille *et al.*, 2015).
235 These values are greater than the concentrations used in the present study and clarify the slow kinetics
236 of agglomeration even for the amphiphilic T_{amphi}, as revealed by time-monitored D_h (Fig. S5). The initial
237 agglomeration/aggregation of the suspensions of ENPs was attributed to the dispersion protocol that
238 may not be energetic enough to reach a dispersion state of individual primary particles. However, such
239 "ideal" dispersion is unrealistic, as suggested by the size of the UV-filters dispersed in sunscreens
240 (Catalano *et al.*, 2020) and the colloidal byproducts a few hundreds of nm observed after dispersion of
241 sunscreens in an aqueous environment (Labille *et al.*, 2010).

242 ZP was little influenced by the electrolyte concentration. Only a small decrease in the absolute ZP value
243 was observed with increasing ionic strength, reflecting the electrical double layer compression.
244 Conversely, it was clearly dependent on the pH. The isoelectric point (IEP) of T_{rutile} was close to 5.7, in
245 agreement with literature data (Kosmulski, 2016, Parks, 1965). The ZP of T_{hydro} was negative at both

246 investigated pHs, as expected by its coating of pure silica (IEP < 3 (Parks, 1965, Kosmulski, 2016)).
247 According to the ZP values in Table 1, the IEP of T_{amphi} was close to 7. This value can be assigned to
248 alumina (IEP ~ 7 - 9 (Kosmulski, 2016, Parks, 1965)), with a likely contribution of the organosilicon layer.
249 This outer layer may screen the underlying aluminol sites and/or contribute to the overall surface
250 charge by the presence of SiO_2 embedded in the polymer, although this mineral was not detected in a
251 previous study by Catalano et al. (Catalano *et al.*, 2020). It may also break up and be partially removed
252 as it was suspected to be only weakly adsorbed (Catalano *et al.*, 2020), but to a limited extent in the
253 present experiments given the time and conditions of sample preparation.

254 Due to the limited sensitivity of DLS that requires concentrations in the mg L^{-1} for reliable estimates of
255 D_h, spICPMS was implemented to investigate the size distribution of the ENPs in suspension. The
256 optimized injected concentrations to avoid particle coincidence detection were between 0.2 and 1 µg
257 L^{-1}. Examples of spICPMS size distributions are provided in Fig. S6 (reference, left panels). The
258 diameters were smaller than the hydrodynamic diameters for the three ENPs, with values ranging from
259 108 to 163 nm (Table 1). Some marginal clusters up to 600-700 nm in diameter were found in the size
260 distribution histograms in Fig. S6 (see also TEM images in Fig. S1). Comparison with the sizes of the
261 primary particles obtained by TEM suggests that the suspensions were probably little agglomerated at
262 trace levels (< µg L^{-1}). However, spICPMS provides mass-equivalent diameters and supposes plain
263 equivalent particle core, thereby underestimating the real size of loose agglomerates/aggregates,
264 whereas DLS, based on the intensity of light scattered by the particles, tends to overestimate it. Given
265 the morphology of the clusters observed by TEM (Fig. S1), it was assumed that D_h best approximated
266 the "real" size of the suspended colloids.

267 3.2. Sand characterization

268 The sand was observed by SEM to check its homogeneity and the aspect of the grain surface. Despite
269 the cleaning process, a few scattered stacked kaolinite platelets were found in cracks and cavities on
270 some of the quartz grains. The sand ZP was negative under all conditions tested (pHs higher than the

IEP of quartz), with smaller negative values in 10^{-2} M NaCl due to the double-layer compression with ionic strength (Table 1).

ICPMS calibration

A previous study has pointed out the differentiated efficiencies of atomization/ionization in the plasma of an ICPMS according to the nature of the particles (Motellier *et al.*, 2014). The ICPMS sensitivity regarding ^{47}Ti for T_{rutile}, T_{hydro}, and T_{amphi} was established by measuring the slope of their calibration curves and comparing them to that obtained with an ionic Ti standard, after correction of the Ti content in each ENP, i.e. excluding coating contribution. As expected, the ICPMS sensitivity factors were lower for Ti in the ENP forms than in the ionic form: T_{rutile} (94%) > T_{hydro} (74%) ~ T_{amphi} (72%). These correction factors were taken into account in the calibration of spICPMS for the online measurements of the ENP concentration and size in the column effluent.

3.3. Column experiments

The ICPMS signals of ^{79}Br, ^{47}Ti, ^{29}Si and ^{27}Al were recorded as a function of time after injection of the samples to evaluate the quantity of ENPs recovered in the column outflow. Examples of BTCs of the three ENPs in 10^{-2} M NaCl at pH 5.7 are provided in Fig. 2. The ICPMS signal of ^{79}Br exhibited a classical shape of BTCs with a plateau representative of the concentration of Br^- in the injected sample. The curve was shifted by ca. 1.15 pore volume in the experiments with the packed column, corresponding to the pore volume of the sand bed and the extra dead volume of the adjustable column end-piece. No other changes of the curve shape were observed, which confirmed the inertness of this ion regarding the collector. The signal of ^{47}Ti was much noisier, reflecting the particulate nature of this analyte. For T_{amphi}, the signal of ^{47}Ti standing for the TiO_2 core and that of ^{27}Al standing for the alumina layer of the coating fitted perfectly (Fig. 2c), which is an argument for the preservation of the coating in the course of the particle transfer through the sand. The background signal of ^{29}Si was high due to the ICPMS sample introduction system and torch materials. Only a small increase at the beginning of the Ti breakthrough in the case of T_{hydro} (Fig. 2b) denoted the silica coating of this ENP. Note that the

296 ICPMS signal began its rise and decrease from the plateau earlier for the ENPs than for the conservative
297 tracer Br^-. This phenomenon occurred both with and without the sand-packed column. It was therefore
298 not related to size exclusion processes in the porous medium but supposed to result from inertial
299 focusing (Martel & Toner, 2014). In the case of particles flowing through a circular cross-sectional
300 channel, this phenomenon induces dynamic grouping of the particles to form an annulus of equilibrium
301 positions towards the center of the stream where the flow is the fastest. In the same conditions, the
302 concentration of ionic species remains homogeneous throughout the cross section of the capillaries.

303 The shift in time of Ti elution with the sand-filled column was identical to that observed with Br^- but
304 the plateau leveled down more or less severely. This decrease in the effluent concentration quantifies
305 the partitioning between the ENPs retained in the sand bed and those leaving the column in the eluting
306 carrier.

307 The C/C_0 ratios between ^{47}Ti signal on the plateau of the BTCs obtained with/without the sand-packed
308 column were plotted as a function of the carrier pH and ionic strength (Fig. 3). Ti recoveries calculated
309 from the BTCs were in a large range (16% - 99%), in line with previous studies on the transfer of TiO_2
310 ENPs through porous media. High (Choy *et al.*, 2008, Petosa *et al.*, 2012, Chen *et al.*, 2011) and low
311 (Guzman *et al.*, 2006, Ben-Moshe *et al.*, 2010) retentions were explained by the favorable or
312 unfavorable deposition conditions in the mechanism of filtration or by physical straining due to the
313 formation of large aggregates and/or the morphology of the collector.

314 Significant differences in the transport behavior through the sand column were observed for the three
315 ENPs. T_{amphi} displayed the highest retention of all (84% in mass) in 10^{-2} M NaCl at pH 5.7. Conversely,
316 T_{hydro} was the most mobile ENP whatever the conditions, with 60% or more of the injected
317 concentration of this UV-filter transferred through the sand. This boosted mobility was attributed to
318 the high repulsive electrostatic forces between the ENP and the collector induced by the substantial
319 negative surface charge of the SiO_2 coating whatever the pH compared to that of T_{rutile} bare TiO_2. These
320 results are in agreement with the findings of Englehart et al. (Englehart *et al.*, 2016) who observed an

increase in TiO_2 mobility through a sand-packed column when TEGO, an acrylate/C10-C30 alkyl acrylate crosspolymer used in commercial suncare products for emulsion thickening, was introduced in the system. Likewise, Petosa et al. (Petosa *et al.*, 2012) and Joo et al. (Joo *et al.*, 2009) emphasized the increase in mobility through sand-packed columns of TiO_2 nanoparticles coated with partially crosslinked polyacrylic acid or carboxymethylcellulose, respectively, compared to their bare counterparts. They attributed this phenomenon to the electrosteric stabilizing property of the polymer surface layers (increase in absolute surface charge) preventing aggregation and subsequent straining.

An important increase in mobility with the pH was observed for all types of TiO_2 nanoparticles. The extent of this phenomenon was dependent on the ENP and the ionic strength. It was the largest with T_{amphi} in 10^{-2} M NaCl (5 fold increase) and the smallest for T_{hydro} which ZP was the least altered by pH changes. Note that the transfer of the ENPs was close to completion in 10^{-3} M NaCl at pH 7.8 whatever the nature of their surface. Chen et al. (Chen *et al.*, 2012) studied the transfer of bare TiO_2 nanoparticles in sand in conditions close to those investigated here. The authors mentioned that the particles were mostly retained at pH 5.7 in eluents composed of NaCl of concentrations greater than 10^{-3} M, in contradiction with the results of the present study where all TiO_2-based ENPs showed a significant transfer through the column at this pH. However, the injected ENP concentration was 200 times higher in the study of Chen et al. and may have accounted for greater homo-aggregation and straining.

All three ENPs were more retained in the column with the highest eluent concentration, in agreement with the general trend reported in the literature (Legg *et al.*, 2014, Chowdhury *et al.*, 2011, Petosa *et al.*, 2012). Again, T_{amphi} showed the greatest dependence on the ionic strength with a three-fold increase of C/C_0 at pH 5.7.

Since the sand collector was negatively charged in all conditions investigated, a plot of C/C_0 as a function of the ZP of the particles was drawn to assess the role of the electrostatic repulsion/attraction at the collector/particle interface (Fig. 4). The two sets of T_{rutile} and T_{hydro} data displayed the same linear

negative correlation. Concerning T_{amphi}, one would expect a severe decrease of C/C_0 as the particle ZP becomes positive (favorable conditions of attachment). Excluding the condition of the highest retention (10^{-2} M NaCl at pH 5.7) which will be discussed thereafter, a linear relationship parallel to- but shifted from the joint correlation line of T_{rutile} and T_{hydro} also emerged, as a first indication of the different deposition behaviors of the primarily hydrophilic ENPs on the one side and the amphiphilic ENP on the other side. The expected severe decrease did occur but when T_{amphi} ZP exceeded 25 mV. For this ENP, it is hypothesized that ZP was governed by the Al_2O_3 internal coating layer, which provides most of the surface charges, as confirmed by its IEP close to that of alumina. Alternatively, C/C_0 was supposed to be markedly influenced by the external polysiloxane layer via the steric hindrance it causes in the interaction process between the particle and the sand collector. The resulting additional repulsion in unfavorable conditions of deposition (ENP ZP < 0) and superposed repulsion to electrostatic attraction in favorable conditions (ENP ZP > 0) can contribute to the shift of T_{amphi} data compared to T_{rutile} and T_{hydro} data in Fig. 4.

Based on data from the BTCs, the maximum transport distance was calculated (Table 2). The short length of the column leads to highly dispersed estimates in conditions where the particles were very mobile. However, small columns have been shown to ameliorate the porous bed homogeneity and limit problems of grain size fractionation that may end up in higher rates of removal via unintended straining (Harvey *et al.*, 1993). The calculated values of the maximum distance reached by the ENPs suggest that the contamination should remain close to its source, from tens of centimeters to tens of meters, unless other conditions likely to boost particle transport are encountered in the vicinity. Such conditions include changes of the environmental medium or the occurrence of preferential flow pathways like rock fractures (Ollivier *et al.*, 2018). The maximum transport distances in the present study are in the range found by Godinez et al. in sand (Godinez & Darnault, 2011) and Fang et al. in natural soils (Fang *et al.*, 2009).

The particle attachment efficiencies α are provided in Table S5. In the conditions of greatest retention (10^{-2} M NaCl, pH 5.7), α was found to be greater than 1 for T_{amphi}, which is an unexpected value when the calculation considers the classical colloid filtration model, where deposition is driven by attachment only. Here, the experimental conditions corresponding to such retention yielded opposite ZP between the sand (ZP < 0) and T_{amphi} (ZP > 0) (Table 1), which should induce an attachment efficiency value close to one. Values of $\alpha \geq 1$ have already been reported in the literature (Godinez & Darnault, 2011, Petosa *et al.*, 2012) and were assigned to additional removal mechanisms. Straining, for instance, can affect the transport of the particles in the sand (Wang *et al.*, 2016, Bradford *et al.*, 2002) and contribute to decrease C/C_0 thus increasing α calculated from this experimental ratio after Eq. 1. Bradford et al. suggested that the colloid attachment theory should be considered with much caution when $d_p/d_{50,collector}$ is greater than a threshold value of 0.0017 because straining can no longer be neglected in this case (Bradford *et al.*, 2002). However, the $d_p/d_{50,collector}$ threshold is expected to depend on the heterogeneity (morphology, surface roughness, size range) of the collector. In their study on the transport of TiO_2 ENPs through a saturated sand column, Godinez et al. (Godinez & Darnault, 2011) calculated attachment efficiencies high above 1 (up to 7.5), suggesting straining contribution to the retention process although their dispersion/collector system obeyed the rule proposed by Bradford et al. In the present study, application of the proposed threshold of 0.0017 with a $d_{50,collector}$ of 235 µm yields d_p values larger than 400 nm for significant straining mechanism to occur. The size distributions of the ENP suspensions (Fig. S4) do show some contribution of particles larger than 400 nm to the total populations but not specific to T_{amphi}. The findings of Legg et al. may also be considered to explain the peculiar retention of T_{amphi} (Legg *et al.*, 2014). They observed that low-density ferrihydrite fractal aggregates can collapse into denser clusters and form thick, localized, unstable deposits that make transport less predictable as the ionic strength increases. Likewise, destabilization of suspended TiO_2 ENPs was found to occur during transport experiments through a sand column in conditions where particle-particle interaction was less repulsive than particle-sand interaction, leading to concurrent aggregation to deposition processes (Solovitch *et al.*, 2010). Such morphological

396 reorganization of T_{amphi} clusters during the transfer with the mediation of the porous medium is
397 plausible and would result in increased straining of the largest clusters grown in-situ.

398 In order to check the possible alteration of the size distribution of the ENPs during their transfer
399 through the column, online spICPMS was implemented. The injected concentration had to be
400 decreased to 2 µg L^{-1} to allow for proper measurement conditions on the breakthrough plateau.
401 Examples of the TiO_2 mass-based size distributions of the injected suspensions (reference, left panels)
402 and of the effluent on the breakthrough plateau (right panels) are provided in Fig. S6. The size
403 distributions of T_{rutile} and T_{hydro} were not significantly different in the injected sample and in the column
404 effluent, meaning that all sizes were affected more or less the same by the deposition process in the
405 sand. These results are different from those of Fang et al. who observed the appearance of a second
406 population of larger size in the column effluent than that of the inflow nano-TiO_2 suspension (Fang *et*
407 *al.*, 2009). This discrepancy was assigned to the much higher injected concentration (20 to 50 mg L^{-1})
408 and to the nature of the collector, i.e. natural soils that are more apt to generate heteroaggregates
409 with some of their constituents (like organic matter, clays, or metal oxides) than the cleaned sand in
410 the present study. However, the hypothesis of Fang et al. suggesting that the kinetics of ENP
411 aggregation was favored by the interactions between them and the soil can explain the increase in the
412 number of aggregates larger than 200 nm and the overall shift towards larger sizes of the outflowing
413 population of T_{amphi} (Fig. S6, bottom) in 10^{-2} M NaCl at pH 5.7. If such online aggregation occurred, it
414 would partly elucidate the aberrant value of the attachment efficiency ($\alpha > 1$) in these experimental
415 conditions.

416 Batch experiments were carried out to spot the adsorption sites of the sand in contact with a
417 suspension of the ENPs. Representative SEM images are provided in Fig. S7. All types of ENPs were
418 almost exclusively deposited as small aggregates (100-300 nm) on the quartz phase; only a few
419 aggregates were found on the residual kaolinite platelets.

3.4. Confrontation of experimental results with DLVO predictions

The overall particle-particle and particle-collector interaction energy was calculated according to Eq. 2 in for T_{rutile} and T_{hydro}. Since the outer coating of T_{amphi} was suspected to take part in the unexpectedly high transfer rate of this ENP through the sand bed, Eq. 3 was also considered hereafter for this ENP to include the contribution of the steric interaction energy. The objective was to elucidate the contrasted deposition and transfer behaviors observed between the investigated ENPs based on the nature of their surface. In a first approach, quartz was supposed to be the main contributor to ENP attachment to the sand. However, since a few ENPs were observed on kaolinite platelets, DLVO calculations involving the possibility for the TiO_2 particles to attach to this mineral (alumina face) were also performed.

Fig. 5 illustrates the interaction energy profiles between a particle and a sand grain surface (quartz) in the different experimental conditions investigated. The particle-particle and particle-kaolinite interaction energy profiles are displayed in Fig. S8.

Agglomeration was favorable for T_{rutile} whereas it was unfavorable - although to a limited extent, particularly at pH 5.7 - for T_{hydro} due to the higher electrostatic repulsion between the negatively charged surfaces of the latter (Fig. S8 a and c). In the case of T_{amphi}, agglomeration was found to be slightly unfavorable, and this tendency was enhanced by considering the contribution of steric repulsion in the model. Agglomeration/aggregation kinetics in 10^{-2} M NaCl at pH 5.7 observed in Fig. S5 qualitatively obeyed the DLVO theory with rather stable suspensions of small aggregates for all three ENPs.

When quartz was considered as the collector, unfavorable deposition conditions were encountered whatever the ionic strength for T_{rutile} at pH 7.8 and T_{hydro} at both pHs (Fig. 5 a and b). A DLVO repulsive barrier ranging from 50 to 320 k_BT was obtained with a maximum magnitude at separation distances of 1 to 5 nm. These values are substantially greater than the kinetic energy of a Brownian particle (~ 1 k_BT) and predict little or no attachment of the TiO_2 ENPs in the primary energy minimum at the surface

of the quartz grains by diffusion only (Shen *et al.*, 2007). However, repulsive energy barrier higher than 800 k_BT have been reported to be overcome (Wang *et al.*, 2011), notably when the shape of the particulate entity is elongated and the interaction via the pointed tips can decrease the energy maximum (Hermansson, 1999). Besides, DLVO theory assumes static conditions. In transport experiments, the conditions become more complicated with the addition of hydrodynamic interactions exerted by the eluent shear flow on the particles at the collector surface (Adamczyk & Weroński, 1999, Chowdhury *et al.*, 2011) which results in a substantial decrease in the energy barrier height (Zaccone *et al.*, 2009). These considerations corroborate the fact that unfavorable attachment conditions limit the retention of the hydrophilic T_{rutile} and T_{hydro} in the sand column but do not exclude them totally from adhering onto the sand surface, as demonstrated by the transfer recoveries (≥ 60%) in Fig. 3. Favorable deposition conditions were obtained for T_{rutile} at pH 5.7, in agreement with the proximity of its IEP which resulted in the lowest recovery of the two hydrophilic ENPs (~ 40%).

When DLVO energy calculation excluding steric interactions from the simethicone layer was considered, favorable deposition conditions on quartz were obtained for T_{amphi} in all experimental conditions but 10^{-3} M NaCl at pH 7.8, for which a low energy barrier (~ 20 k_BT) was obtained. These energy profiles could not account for the unexpectedly high mobility of T_{amphi} through the sand column, especially at the lowest ionic strength. Consideration of the steric hindrance from the viscoelastic PDMS created a gradual increase of the interaction energy at approaching distance closer than the layer thickness (7 nm here) in all conditions but 10^{-3} M NaCl at pH 5.7 (Fig. 5 a). In this latter eluent condition, the particle size of the aggregates was too small (D_h = 92 ± 5 nm, Table 1) to induce a net positive interaction energy. For all other conditions, the steric contribution masked the primary minimum and shifted the attachment condition from favorable to unfavorable. Comparing Fig. 5 a and b, one would expect the mobility of T_{amphi} to increase when shifting the NaCl concentration from 10^{-3} M NaCl to 10^{-2} M NaCl at pH 5.7, should the steric hindrance be determinant. However, C/C_0 decreased to its lower value, leading to a calculated value of $\alpha > 1$, and consolidating the hypothesis of an additional deposition mechanism in the condition of greatest retention for T_{amphi}. DLVO theory is not

always successful in predicting the attachment of particles in porous media (Elimelech & O'Melia, 1990) when kinetics needs to be considered. Shearing forces induced by high flow velocities have been reported to accelerate the rate of homoaggregation (Zaccone *et al.*, 2009) or, conversely, to break up the attached aggregates and decrease their size (Chowdhury *et al.*, 2011). Opposite consequences are deduced from these possible mechanisms, including straining or better pore accessibility (enhanced immobilization), or size exclusion (enhanced transfer). The small overall increased size of the T_{amphi} population eluted from the column may account for an intra-column-promoted gradual aggregation leading to straining of the larger, newly-formed clusters.

Kaolinite is a residual secondary mineral phase located in remote places of the sand grains. According to the DLVO theory, attachment of the ENPs on kaolinite was favored at pH 5.7 (Fig. S8 b and d). Should the interaction with kaolinite be prevalent, the elution of the ENPs from the column would be very limited, which is in contradiction with the recoveries obtained for all three ENPs and with SEM observations. Although the stacked clay platelets may have accounted for local deposits, they played a limited role in the retention of TiO_2-based ENPs, in contrast with its significant contribution brought out in previous transport experiments with gold nanoparticles in the same porous medium (Motellier *et al.*, 2019). The coupled effects of hydrodynamics and sand grain surface roughness, creating a shadow effect (Ko & Elimelech, 2000, Sasidharan *et al.*, 2014), or the fact that the constituent minerals create heterogeneities at the microscale with a possible “hydrodynamic bump” effect (Elimelech *et al.*, 2003) may also contribute to the poor impact of kaolinite on the retention of the TiO_2-based ENPs in the sand bed.

The Boltzmann factor and Maxwell models both predict a linear relationship independent of the experimental conditions between α and $\exp(-E_{max})$ (Shen *et al.*, 2007). A barrier-controlled regime of deposition was observed in the case of T_{rutile} and T_{hydro} (Fig. 6). The same correlation factor was obtained for T_{rutile} and T_{hydro} with a shift towards higher E_{max} for the latter, meaning that the silica-coated hydrophilic ENP could overcome higher energy barrier heights than its naked TiO_2 ENP

counterpart to attach in the primary minimum. Log(α) obeyed a higher degree of dependence on E_{max} for T_{amphi}, which suggests that the alumina/simethicone-coated amphiphilic ENP was not able to overcome low energy barrier heights for attachment and justifies the consideration of the role of PDMS in the ENP-collector repulsion. Overall, Fig. 6 shows that the retention behavior derived from particle-collector interactions of the bare TiO_2 ENP (T_{rutile}) was intermediate between that of the hydrophilic-coated TiO_2 ENP (T_{hydro}) and that of the amphiphilic-coated TiO_2 ENP (T_{amphi}).

4. Conclusion

The results of the present study suggest that a fraction of the particle population can still migrate through the porous medium even in favorable deposition conditions when no repulsive barriers between the particles and the sand collector are encountered. This unexpected spread of the contamination is assumed to increase with the shear flow unless concurrent aggregation processes promote straining and subsequent immobilization of the ENPs. The amphiphilic UV-filter showed a distinct transport behavior compared to its bare and hydrophilic counterparts. Despite general favorable attachment conditions considering DLVO theory and probable in-situ agglomeration/aggregation in particular conditions (high ionic strength), significant transfer (16 – 95%) through the sand was observed for this ENP, tentatively assigned to screening/steric effects resulting from its polysiloxane coating. This study confirms that the interactions between a mineral nanoparticulate UV-filter and a porous medium acting as collector cannot be properly described by a bare TiO_2 ENP surrogate. Depending on the nature of the UV-filter coating and the physico-chemical conditions, retention can be either enhanced or reduced compared to uncoated TiO_2 ENPs. The environmental implication of these results is a larger but probably circumscribed contamination beyond attended recreational areas compared to the mostly localized one expected with uncoated TiO_2 ENPs used in most studies. The design of nanoparticulate UV-filters –and particularly the nature

of their coating- should take into account their environmental fate and their transfer through sand/soils surrounding places of high use of sunscreens to promote sustainable product formulations.

Acknowledgements

The authors wish to thank Rémi Béra for providing the cleaned sand.

Formatting of funding sources

This work is a contribution to the LABEX SERENADE (ANR-11-LABX-0064) funded by the Investissements d'Avenir", a French Government program of the French National Research Agency (ANR) through the A*Midex project ECOSUN (ANR-11-IDEX-0001-02). TEM and ICPMS equipment are part of the NanoID platform supported by the French Investissement d'Avenir ANR-10-EQPX-39.

References

Adamczyk, Z. & Weroński, P. (1999). *Advances in Colloid and Interface Science* **83**, 137-226.
Ben-Moshe, T., Dror, I. & Berkowitz, B. (2010). *Chemosphere* **81**, 387-393.
Botta, C., Labille, J., Auffan, M., Borschneck, D., Miche, H., Cabié, M., Masion, A., Rose, J. & Bottero, J.-Y. (2011). *Environmental Pollution* **159**, 1543-1550.
Bradford, S. A., Sasidharan, S., Kim, H., Gomez-Flores, A., Li, T. & Shen, C. (2021). *Langmuir* **37**, 1501-1510.
Bradford, S. A., Yates, S. R., Bettahar, M. & Simunek, J. (2002). *Water Resources Research* **38**, 63-61-63-12.
Byrd, T. L. & Walz, J. Y. (2005). *Environmental Science & Technology* **39**, 9574-9582.
Cai, L., Tong, M., Wang, X. & Kim, H. (2014). *Environmental Science & Technology* **48**, 7323-7332.
Cary, L., Pauwels, H., Ollivier, P., Picot, G., Leroy, P., Mougin, B., Braibant, G. & Labille, J. (2015). *Journal of Contaminant Hydrology* **179**, 148-159.
Catalano, R., Masion, A., Ziarelli, F., Slomberg, D., Laisney, J., Unrine, J. M., Campos, A. & Labille, J. (2020). *Colloids and Surfaces A: Physicochemical and Engineering Aspects* **599**, 124792.
Catalano, R., Slomberg, D., Picard, C., Hucher, N., Vidal, V., Saint-Antonin, F., Hubaud, J.-C., Rose, J. & Labille, J. (2021). *Environmental Science: Nano* **Accepted**.
Chen, G., Liu, X. & Su, C. (2011). *Langmuir* **27**, 5393-5402.
Chen, G., Liu, X. & Su, C. (2012). *Environmental Science & Technology* **46**, 7142-7150.

552 Chowdhury, I., Hong, Y., Honda, R. J. & Walker, S. L. (2011). *Journal of Colloid and Interface Science*
553 **360**, 548-555.
554 Choy, C. C., Wazne, M. & Meng, X. (2008). *Chemosphere* **71**, 1794-1801.
555 Danovaro, R., Bongiorni, L., Corinaldesi, C., Giovannelli, D., Damiani, E., Astolfi, P., Greci, L. &
556 Pusceddu, A. (2008). *Environmental Health Perspectives* **116**, 441-447.
557 de Buyl, F. (2001). *International Journal of Adhesion and Adhesives* **21**, 411-422.
558 Elimelech, M., Chen, J. Y. & Kuznar, Z. A. (2003). *Langmuir* **19**, 6594-6597.
559 Elimelech, M. & O'Melia, C. R. (1990). *Environmental Science & Technology* **24**, 1528-1536.
560 Englehart, J., Lyon, B. A., Becker, M. D., Wang, Y., Abriola, L. M. & Pennell, K. D. (2016).
561 *Environmental Science: Nano* **3**, 157-168.
562 Fang, J., Shan, X.-q., Wen, B., Lin, J.-m. & Owens, G. (2009). *Environmental Pollution* **157**, 1101-1109.
563 Faure, B., Salazar-Alvarez, G., Ahniyaz, A., Villaluenga, I., Berriozabal, G., De Miguel, Y. R. &
564 Bergström, L. (2013). *Science and Technology of Advanced Materials* **14**, 023001.
565 Godinez, I. G. & Darnault, C. J. G. (2011). *Water Research* **45**, 839-851.
566 Gondikas, A., von der Kammer, F., Kaegi, R., Borovinskaya, O., Neubauer, E., Navratilova, J.,
567 Praetorius, A., Cornelis, G. & Hofmann, T. (2018). *Environmental Science: Nano* **5**, 313-326.
568 Gondikas, A. P., Kammer, F. v. d., Reed, R. B., Wagner, S., Ranville, J. F. & Hofmann, T. (2014).
569 *Environmental Science & Technology* **48**, 5415-5422.
570 Gottschalk, F., Sun, T. & Nowack, B. (2013). *Environmental Pollution* **181**, 287-300.
571 Guzman, K. A. D., Finnegan, M. P. & Banfield, J. F. (2006). *Environmental Science and Technology* **40**,
572 7688-7693.
573 Harvey, R. W., Kinner, N. E., MacDonald, D., Metge, D. W. & Bunn, A. (1993). *Water Resources*
574 *Research* **29**, 2713-2721.
575 Hermansson, M. (1999). *Colloids and Surfaces B: Biointerfaces* **14**, 105-119.
576 Johnson, A. C., Bowes, M. J., Crossley, A., Jarvie, H. P., Jurkschat, K., Jürgens, M. D., Lawlor, A. J., Park,
577 B., Rowland, P., Spurgeon, D., Svendsen, C., Thompson, I. P., Barnes, R. J., Williams, R. J. & Xu,
578 N. (2011). *Science of The Total Environment* **409**, 2503-2510.
579 Johnston, H. J., Hutchison, G. R., Christensen, F. M., Peters, S., Hankin, S. & Stone, V. (2009). *Particle*
580 *and Fibre Toxicology* **6**, 33.
581 Joo, S. H., Al-Abed, S. R. & Luxton, T. (2009). *Environmental Science & Technology* **43**, 4954-4959.
582 Keller, A. A., McFerran, S., Lazareva, A. & Suh, S. (2013). *Journal of Nanoparticle Research* **15**, 1692.
583 Keller, A. A., Wang, H., Zhou, D., Lenihan, H. S., Cherr, G., Cardinale, B. J., Miller, R. & Ji, Z. (2010).
584 *Environmental Science & Technology* **44**, 1962-1967.
585 Ko, C.-H. & Elimelech, M. (2000). *Environmental Science & Technology* **34**, 3681-3689.
586 Kosmulski, M. (2016). *Advances in Colloid and Interface Science* **238**, 1-61.
587 Labille, J., Catalano, R., Slomberg, D., Motellier, S., Pinsino, A., Hennebert, P., Santaella, C. &
588 Bartolomei, V. (2020). *Frontiers in Environmental Science* **8**.
589 Labille, J., Feng, J., Botta, C., Borschneck, D., Sammut, M., Cabie, M., Auffan, M., Rose, J. & Bottero, J.-
590 Y. (2010). *Environmental Pollution* **158**, 3482-3489.
591 Labille, J., Harns, C., Bottero, J.-Y. & Brant, J. (2015). *Environmental Science & Technology* **49**, 6608-
592 6616.
593 Labille, J., Slomberg, D., Catalano, R., Robert, S., Apers-Tremelo, M. L., Boudenne, J. L., Manasfi, T. &
594 Radakovitch, O. (2020). *The Science of the total environment* **706**, 136010.
595 Legg, B. A., Zhu, M., Comolli, L. R., Gilbert, B. & Banfield, J. F. (2014). *Environmental Science &*
596 *Technology* **48**, 13703-13710.
597 Lewicka, Z. A., Benedetto, A. F., Benoit, D. N., Yu, W. W., Fortner, J. D. & Colvin, V. L. (2011). *Journal*
598 *of Nanoparticle Research* **13**, 3607.
599 Li, L., Sillanpää, M. & Risto, M. (2016). *Environmental Pollution* **219**, 132-138.
600 Li, S., Wallis, L. K., Ma, H. & Diamond, S. A. (2014). *Science of The Total Environment* **466-467**, 800-
601 808.
602 Lv, X., Gao, B., Sun, Y., Dong, S., Wu, J., Jiang, B. & Shi, X. (2016). *Science of The Total Environment*
603 **563-564**, 987-995.

Martel, J. M. & Toner, M. (2014). *Annu Rev Biomed Eng* **16**, 371-396.
Motellier, S., Guiot, A., Legros, S. & Fiorentino, B. (2014). *Journal of Analytical Atomic Spectrometry* **29**, 2294-2301.
Motellier, S., Locatelli, D. & Bera, R. (2019). *Environmental Science & Technology* **53**, 10714-10722.
Mueller, N. C. & Nowack, B. (2008). *Environmental Science & Technology* **42**, 4447-4453.
Nikanorov, A. M. & Brazhnikova, L. V. (2009). *Types and properties of water - Volume II*, edited by M. G. Khublaryan, p. 42: EOLSS Publications.
Ollivier, P., Pauwels, H., Wille, G., Devau, N., Braibant, G., Cary, L., Picot-Colbeaux, G. & Labille, J. (2018). *Journal of Hazardous Materials* **359**, 47-55.
Osterwalder, U., Sohn, M. & Herzog, B. (2014). *Photodermatology, Photoimmunology & Photomedicine* **30**, 62-80.
Parks, G. A. (1965). *Chemical Reviews* **65**, 177-198.
Peijnenburg, W., Praetorius, A., Scott-Fordsmand, J. & Cornelis, G. (2016). *Environmental Pollution* **218**, 1365-1369.
Petosa, A. R., Brennan, S. J., Rajput, F. & Tufenkji, N. (2012). *Water Research* **46**, 1273-1285.
Reed, R. B., Martin, D. P., Bednar, A. J., Montaño, M. D., Westerhoff, P. & Ranville, J. F. (2017). *Environmental Science: Nano* **4**, 69-77.
Sánchez-Quiles, D. & Tovar-Sánchez, A. (2014). *Environmental Science & Technology* **48**, 9037-9042.
Sasidharan, S., Torkzaban, S., Bradford, S. A., Dillon, P. J. & Cook, P. G. (2014). *Colloids and Surfaces A: Physicochemical and Engineering Aspects* **457**, 169-179.
Sendra, M., Sánchez-Quiles, D., Blasco, J., Moreno-Garrido, I., Lubián, L. M., Pérez-García, S. & Tovar-Sánchez, A. (2017). *Environment International* **98**, 62-68.
Shen, C., Li, B., Huang, Y. & Jin, Y. (2007). *Environmental Science & Technology* **41**, 6976-6982.
Solovitch, N., Labille, J., Rose, J., Chaurand, P., Borschneck, D., Wiesner, M. R. & Bottero, J.-Y. (2010). *Environmental Science & Technology* **44**, 4897-4902.
Stokes, R. P. & Diffey, B. L. (1999). *The British journal of dermatology* **140**, 259-263.
Tovar-Sánchez, A., Sánchez-Quiles, D., Basterretxea, G., Benedé, J. L., Chisvert, A., Salvador, A., Moreno-Garrido, I. & Blasco, J. (2013). *PLOS ONE* **8**, e65451.
Tufenkji, N. & Elimelech, M. (2004). *Environmental Science & Technology* **38**, 529-536.
Venkatesan, A. K., Reed, R. B., Lee, S., Bi, X., Hanigan, D., Yang, Y., Ranville, J. F., Herckes, P. & Westerhoff, P. (2018). *Bulletin of Environmental Contamination and Toxicology* **100**, 120-126.
Vitorge, E. (2010). thesis*,* Université de Grenoble.
Wang, H., Sodagari, M., Chen, Y., He, X., Newby, B.-m. Z. & Ju, L.-K. (2011). *Colloids and Surfaces B: Biointerfaces* **87**, 415-422.
Wang, M., Gao, B. & Tang, D. (2016). *Journal of Hazardous Materials* **318**, 233-246.
Zaccone, A., Wu, H., Gentili, D. & Morbidelli, M. (2009). *Physical Review E* **80**, 051404.
Zhou, D., Ji, Z., Jiang, X., Dunphy, D. R., Brinker, J. & Keller, A. A. (2013). *PLOS ONE* **8**, e81239.

Figures

Transport of nanoparticulate TiO_2 UV-filters through a saturated sand column at environmentally relevant concentrations

Sylvie Motellier[1]*, Amandine Arnould[1], Dominique Locatelli[1], and Jérôme Labille[2]

[1] Univ. Grenoble Alpes, CEA, LITEN, DTNM, STDC, Laboratory of Measure, Safety, and Environment, 38000 Grenoble, France

[2] Aix Marseille Univ, CNRS, IRD, INRAE, Coll France, CEREGE, Aix-en-Provence, France

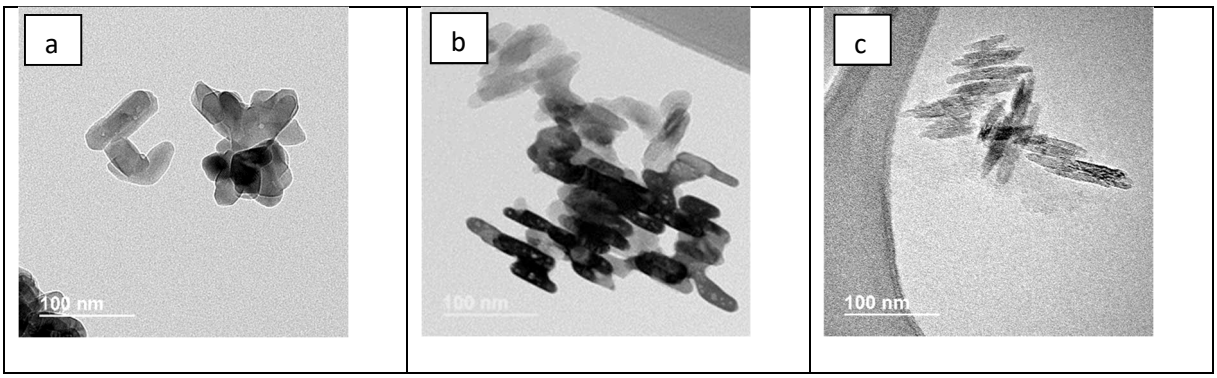

Fig. 1. TEM images of (a) T_{rutile}, (b) T_{hydro}, and (c) T_{amphi}. ENP concentration: 50 mg L^{-1} in UP water.

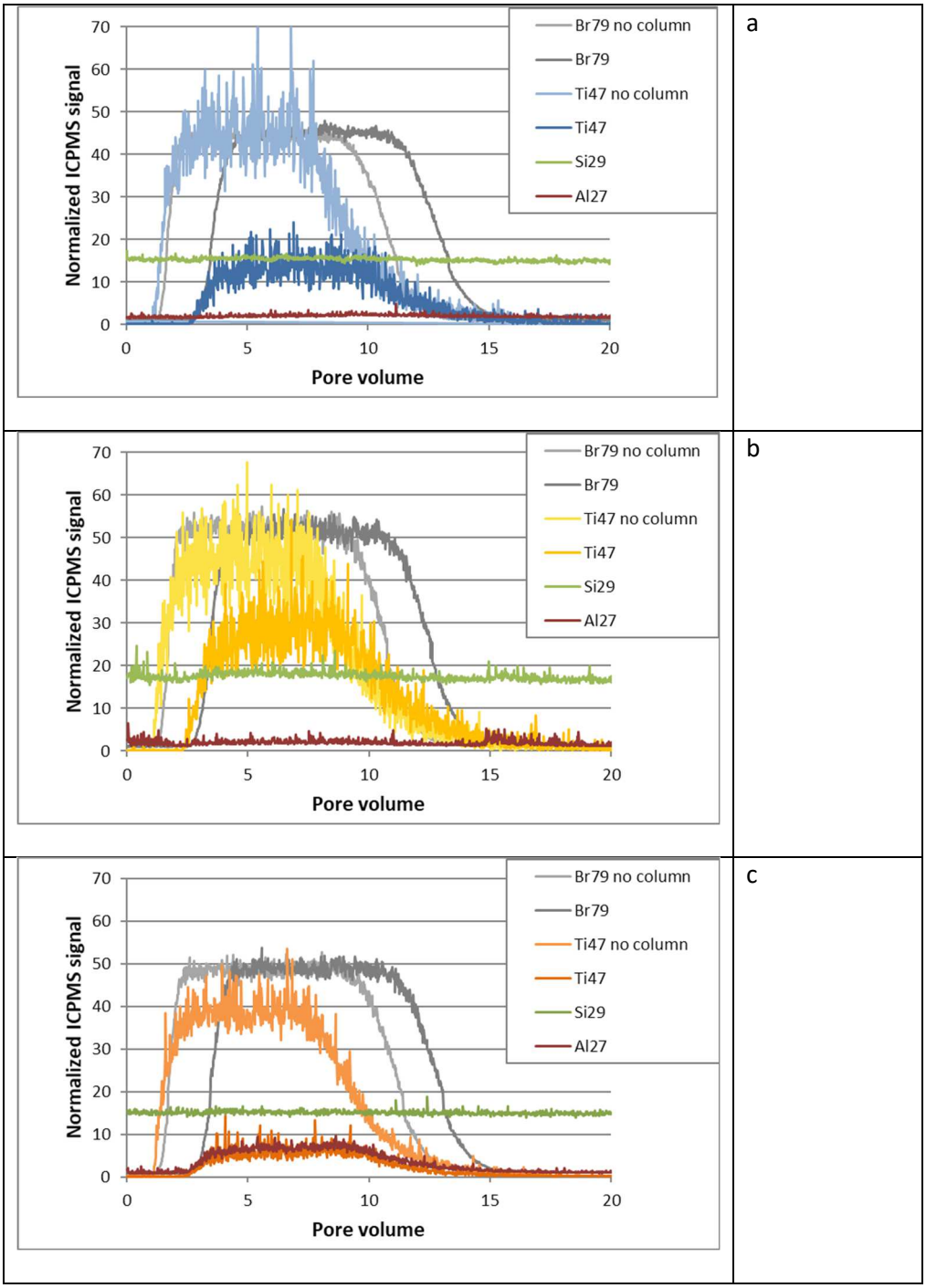

Fig. 2. Examples of Br (non-interacting species), Ti, Si, and Al BTCs in the column effluent monitored by online ICPMS for (a) T_{rutile}, (b) T_{hydro}, and (c) T_{amphi}. Light colors refer to the BTCs without column in the flow stream; darker shades correspond to the BTCs after transfer through the sand bed. Eluent 10^{-2} M NaCl, pH 5.7. Injected ENP concentration: 100 µg L^{-1}.

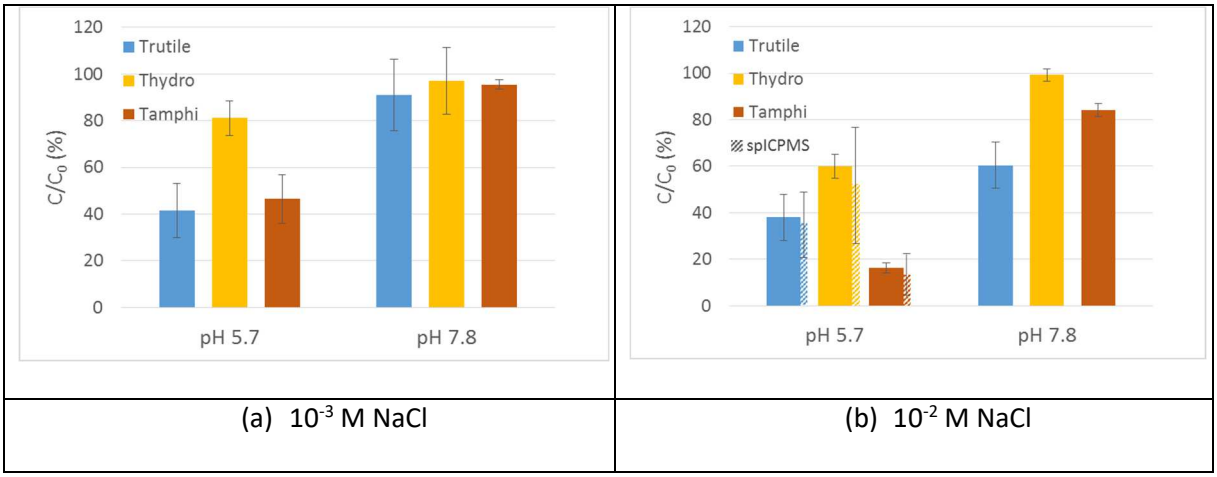

(a) 10^{-3} M NaCl (b) 10^{-2} M NaCl

Fig. 3. Ti mass recovery from ENP breakthrough curves monitored by online ICPMS for eluents composed of (a) 10^{-3} M NaCl and (b) 10^{-2} M NaCl and pHs of 5.7 and 7.8. Injected ENP concentration: 100 µg L^{-1}. Striped columns refer to data from spICPMS (injected concentration 2 µg L^{-1}).

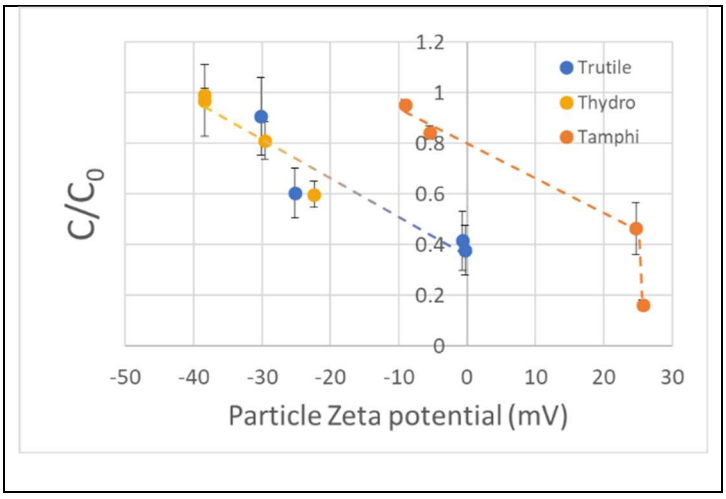

Fig. 4. Influence of the particle Zeta potential on the ENP recovery in the column outflow. Eluent 10^{-3} and 10^{-2} M NaCl, pH 5.7 and 7.8. Injected ENP concentration: 100 µg L^{-1}.

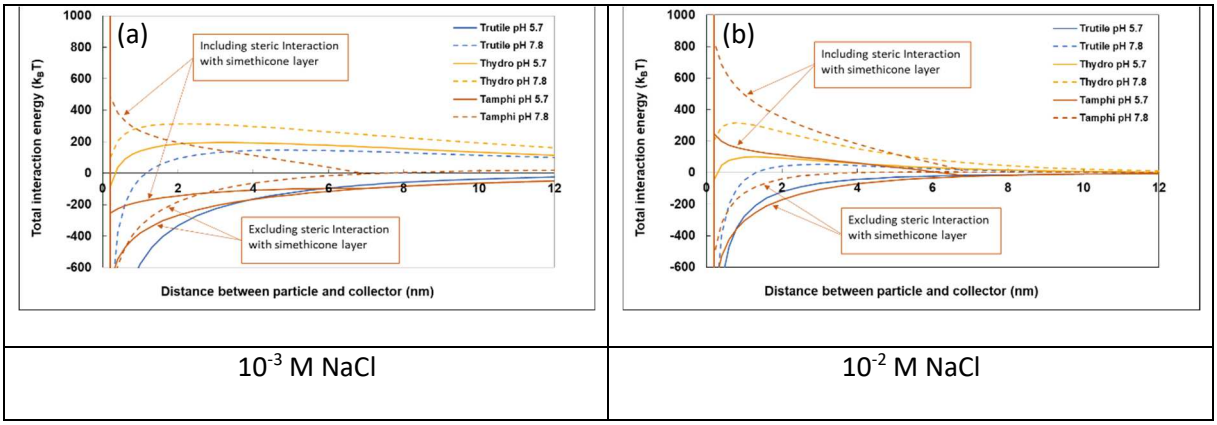

10^{-3} M NaCl	10^{-2} M NaCl

Fig. 5. DLVO interaction energy profiles between the ENPs and quartz in 10^{-3} M NaCl (a) and 10^{-2} M NaCl (b).

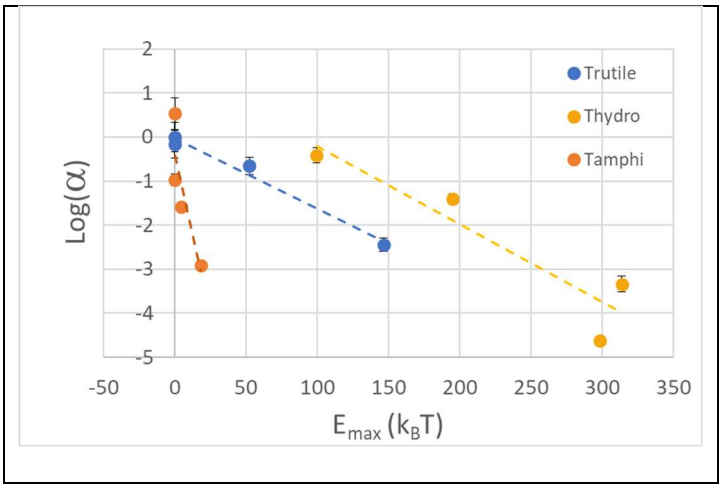

Fig. 6. Influence of the height of the repulsive energy barrier (DLVO) on the attachment efficiency of the ENPs in the packed sand bed.

Tables

Transport of nanoparticulate TiO_2 UV-filters through a saturated sand column at environmentally relevant concentrations

Sylvie Motellier[1]*, Amandine Arnoult[1], Dominique Locatelli[1], and Jérôme Labille[2]

[1] Univ. Grenoble Alpes, CEA, LITEN, DTNM, STDC, Laboratory of Measure, Safety, and Environment, 38000 Grenoble, France

[2] Aix Marseille Univ, CNRS, IRD, INRAE, Coll France, CEREGE, Aix-en-Provence, France

Table 1. ENP characteristics (equivalent average TiO_2 mass-based diameter $D_{spICPMS}$, hydrodynamic diameter (number mean) D_h, and ZP) and sand surface ZP in the selected eluent conditions (10^{-3} and 10^{-2} M NaCl at pH 5.7 and 7.8). ENP concentration: DLS: 2 mg L^{-1}; spICPMS: 0.2 - 1 µg L^{-1}.

		T_{rutile}	T_{hydro}	T_{amphi}	Sand
TEM (n = 20)	Length of primary particles (nm)	64 ± 15	59 ± 8	65 ± 11	
spICPMS NaCl 10^{-2} M, pH 5.7	$D_{spICPMS}$ (nm)	135 ± 5	163 ± 7	108 ± 3	
NaCl 10^{-3} M pH 5.7	D_h (nm) ZP (mV)	217 ± 6 -0.7 ± 1.4	242 ± 3 -29.6 ± 0.4	92 ± 5 24.7 ± 3.0	 -67.8
NaCl 10^{-3} M pH 7.8	D_h (nm) ZP (mV)	204 ± 8 -30.2 ± 1.4	239 ± 25 -38.4 ± 1.0	241 ± 23 -9.1 ± 6.6	 -73.2
NaCl 10^{-2} M pH 5.7	D_h (nm) ZP (mV)	221 ± 11 -0.3 ± 2.0	254 ± 18 -22.4 ± 0.4	173 ± 22 25.7 ± 3.1	 -46.1
NaCl 10^{-2} M pH 7.8	D_h (nm) ZP (mV)	221 ± 16 -25.2 ± 1.7	263 ± 8 -38.4 ± 1.4	208 ± 17 -5.5 ± 1.3	 -63.4

Table 2. Maximum transport distance covered by the ENPs in the experimental conditions of the study.

Maximum transport distance (m)	T_{rutile}	T_{hydro}	T_{amphi}
NaCl 10^{-3} M pH 5.7	0.24 ± 0.08	0.99 ± 0.43	0.27 ± 0.08
NaCl 10^{-3} M pH 7.8	2.2 ± 3.8	6.8 ± 32.7	4.5 ± 2.0
NaCl 10^{-2} M pH 5.7	0.21 ± 0.06	0.40 ± 0.07	0.11 ± 0.01
NaCl 10^{-2} M pH 7.8	0.41 ± 0.13	28 ± 98	1.2 ± 0.2

Graphical abstract

Transport of nanoparticulate TiO_2 UV-filters through a saturated sand column at environmentally relevant concentrations

Sylvie Motellier[1]*, Amandine Arnould[1], Dominique Locatelli[1], and Jérôme Labille[2]

[1] Univ. Grenoble Alpes, CEA, LITEN, DTNM, STDC, Laboratory of Measure, Safety, and Environment, 38000 Grenoble, France

[2] Aix Marseille Univ, CNRS, IRD, INRAE, Coll France, CEREGE, Aix-en-Provence, France